

# Detailed characterization of a laboratory magnetized supercritical collisionless shock and of the associated proton energization

Cite as: Matter Radiat. Extremes **7**, 014402 (2022); <https://doi.org/10.1063/5.0055071>

Submitted: 25 April 2021 • Accepted: 26 September 2021 • Published Online: 08 December 2021

 W. Yao, A. Fazzini, S. N. Chen, et al.

## COLLECTIONS

Paper published as part of the special topic on [Magnetized Plasmas in HEDP](#)

 This paper was selected as Featured



View Online



Export Citation



CrossMark

## ARTICLES YOU MAY BE INTERESTED IN

[Generation of single-cycle relativistic infrared pulses at wavelengths above 20  \$\mu\text{m}\$  from density-tailored plasmas](#)

Matter and Radiation at Extremes **7**, 014403 (2022); <https://doi.org/10.1063/5.0068265>

[Recent progress in matter in extreme states created by laser](#)

Matter and Radiation at Extremes **7**, 013001 (2022); <https://doi.org/10.1063/5.0078895>

[Characterization and performance of the Apollon short-focal-area facility following its commissioning at 1 PW level](#)

Matter and Radiation at Extremes **6**, 064402 (2021); <https://doi.org/10.1063/5.0065138>



Matter and Radiation at Extremes

2022 Topical Webinar Series

[LEARN MORE](#)













# Detailed characterization of a laboratory magnetized supercritical collisionless shock and of the associated proton energization

Cite as: Matter Radiat. Extremes 7, 014402 (2022); doi: 10.1063/5.0055071

Submitted: 25 April 2021 • Accepted: 26 September 2021 •

Published Online: 8 December 2021



W. Yao,<sup>1,2,a)</sup>  A. Fazzini,<sup>1</sup> S. N. Chen,<sup>3</sup> K. Burdonov,<sup>1,2,4</sup> P. Antici,<sup>5</sup>  J. Béard,<sup>6</sup>  S. Bolaños,<sup>1</sup>   
A. Ciardi,<sup>2</sup>  R. Diab,<sup>1</sup>  E. D. Filippov,<sup>7,4</sup>  S. Kisiov,<sup>3</sup> V. Lelasseux,<sup>1</sup>  M. Miceli,<sup>8,9</sup>  Q. Moreno,<sup>10,11</sup>   
V. Nastasa,<sup>3</sup> S. Orlando,<sup>9</sup> S. Pikuz,<sup>7,12</sup> D. C. Popescu,<sup>3</sup>  G. Revet,<sup>1</sup> X. Ribeyre,<sup>10</sup>  E. d'Humières,<sup>10</sup> and J. Fuchs<sup>1</sup>

## AFFILIATIONS

<sup>1</sup>LULI-CNRS, CEA, UPMC Univ Paris 06: Sorbonne Université, Ecole Polytechnique, Institut Polytechnique de Paris, F-91128 Palaiseau Cedex, France

<sup>2</sup>Sorbonne Université, Observatoire de Paris, Université PSL, CNRS, LERMA, F-75005 Paris, France

<sup>3</sup>ELI-NP, "Horia Hulubei" National Institute for Physics and Nuclear Engineering, 30 Reactorului Street, RO-077125 Bucharest-Magurele, Romania

<sup>4</sup>IAP, Russian Academy of Sciences, 603155 Nizhny Novgorod, Russia

<sup>5</sup>INRS-EMT, 1650 Blvd. Lionel-Boulet, Varennes, Quebec J3X 1S2, Canada

<sup>6</sup>LNCMI, UPR 3228, CNRS-UGA-UPS-INSA, F-31400 Toulouse, France

<sup>7</sup>JIHT, Russian Academy of Sciences, 125412 Moscow, Russia

<sup>8</sup>Università degli Studi di Palermo, Dipartimento di Fisica e Chimica E. Segrè, Piazza del Parlamento 1, 90134 Palermo, Italy

<sup>9</sup>INAF-Osservatorio Astronomico di Palermo, Palermo, Italy

<sup>10</sup>University of Bordeaux, Centre Lasers Intenses et Applications, CNRS, CEA, UMR 5107, F-33405 Talence, France

<sup>11</sup>ELI-Beamlines, Institute of Physics, Czech Academy of Sciences, 5 Kvetna 835, 25241 Dolni Brezany, Czech Republic

<sup>12</sup>NRNU MEPhI, 115409 Moscow, Russia

**Note:** This paper is part of the Special Issue on Magnetized Plasmas in HED.

**a)** Author to whom correspondence should be addressed: [yao.weipeng@polytechnique.edu](mailto:yao.weipeng@polytechnique.edu)

## ABSTRACT

Collisionless shocks are ubiquitous in the Universe and are held responsible for the production of nonthermal particles and high-energy radiation. In the absence of particle collisions in the system, theory shows that the interaction of an expanding plasma with a pre-existing electromagnetic structure (as in our case) is able to induce energy dissipation and allow shock formation. Shock formation can alternatively take place when two plasmas interact, through microscopic instabilities inducing electromagnetic fields that are able in turn to mediate energy dissipation and shock formation. Using our platform in which we couple a rapidly expanding plasma induced by high-power lasers (JLF/Titan at LLNL and LULI2000) with high-strength magnetic fields, we have investigated the generation of a magnetized collisionless shock and the associated particle energization. We have characterized the shock as being collisionless and supercritical. We report here on measurements of the plasma density and temperature, the electromagnetic field structures, and the particle energization in the experiments, under various conditions of ambient plasma and magnetic field. We have also modeled the formation of the shocks using macroscopic hydrodynamic simulations and the associated particle acceleration using kinetic particle-in-cell simulations. As a companion paper to Yao *et al.* [Nat. Phys. 17, 1177–1182 (2021)], here we show additional results of the experiments and simulations, providing more information to allow their reproduction and to demonstrate the robustness of our interpretation of the proton energization mechanism as being shock surfing acceleration.

© 2021 Author(s). All article content, except where otherwise noted, is licensed under a Creative Commons Attribution (CC BY) license (<http://creativecommons.org/licenses/by/4.0/>). <https://doi.org/10.1063/5.0055071>

## I. INTRODUCTION

The acceleration of energetic charged particles by a collisionless magnetized shock is a ubiquitous phenomenon in astrophysical environments, in which the most energetic particles are the ultra-high-energy cosmic rays (UHECRs) accelerated in the interstellar medium (ISM).<sup>1,2</sup> In these environments, the sources of collisionless dissipation are self-generated electromagnetic fields, resulting from kinetic instabilities such as the Weibel instability. Particles are also accelerated in the Solar System owing to collisionless magnetized shocks generated by the interaction of the solar wind with planetary magnetospheres<sup>3,4</sup> and, at larger distances, with the ISM.<sup>5</sup> Here, the source of collisionless dissipation is the pre-existing global electromagnetic structure. This will also be the case for the experiment detailed here, where we apply a global strong magnetic field to a laser-ablated fast plasma. Since these shocks usually have a magnetosonic Mach number  $M_{\text{ms}} = v_{\text{sh}}/v_{\text{ms}} \geq 2.7$  (where  $v_{\text{sh}}$  is the shock velocity,  $v_{\text{ms}} = \sqrt{C_s^2 + v_A^2}$  is the magnetosonic velocity, and  $C_s$  and  $v_A$  are the ion sound velocity and Alfvénic velocity, respectively), they belong to the so-called supercritical regime,<sup>6,7</sup> which means that these shocks are not maintained by classical dissipation alone. To help maintain a shock, the additional channel for the expulsion of energy is via reflection of particles back upstream.<sup>8</sup>

A variety of acceleration mechanisms have been invoked as a means to transfer energy from shock waves to particles, including shock surfing acceleration (SSA), shock drift acceleration (SDA), and diffusive shock acceleration (DSA). DSA requires a high initial energy before further acceleration,<sup>9</sup> thus raising the so-called “injection problem,”<sup>10</sup> while SSA and SDA are believed to be responsible for generating the pre-accelerated seed particles, i.e., for the initial process of acceleration from thermal energies. Although it is still under debate whether SSA or SDA dominates the pre-acceleration process in various collisionless shock environments,<sup>11–13</sup> we can distinguish them by the following two aspects. On the one hand, in SSA, charged particles are first reflected at the shock front (owing to the cross-shock potential electric field), and they then surf along the shock front against the convective electric field ( $\mathbf{E} = -\mathbf{v} \times \mathbf{B}$ ), thus gaining energy, while in SDA, charged particles drift (owing to the magnetic field gradient at the shock front) along the convective electric field and then gain energy.<sup>14</sup> On the other hand, SSA requires a shock width that is thin compared with the Larmor radius of the charged particles, while SDA needs the opposite (so that the charged particles can gyrate and drift within the shock layer).<sup>9,15</sup>

However, because of the immense spatial scales involved in collisionless phenomenon (e.g., the mean free path is  $\lambda_{\text{mfp}} \sim 1$  AU in the Solar System), only a very small sampling of the shock formation and dissipation mechanisms can be realized. As a result, we still do not have a full understanding of the formation and evolution of collisionless shocks, and the question of the effectiveness and relative importance of SDA and SSA is still widely debated in the literature.<sup>16</sup> To further our understanding, laboratory experiments (and their simulations) have proved to be an effective tool, providing highly resolved, reproducible, and controllable multidimensional datasets that can complement astrophysical observations.<sup>17,18</sup> Below, we will briefly review the investigation of collisionless shocks via laboratory experiments.

The route that up until now has been most explored in the laboratory is to produce a shock (mediated by the Weibel filamentation instability) by colliding two ablative unmagnetized flows driven by

high-energy nanosecond lasers. This setup has yielded promising results at the Omega Laser Facility<sup>19–21</sup> and the National Ignition Facility (NIF),<sup>22,23</sup> as well as at many other laser facilities all over the world.<sup>24–26</sup> Recently, experiments on collisionless shocks in plasma flows in which there was a significant self-generated magnetic field showed, for the first time, the formation of magnetized collisionless shocks, with the generation of Weibel instability and observation of electron acceleration in the turbulent structure.<sup>27</sup> Most recently, the dynamics of the ion Weibel instability have been characterized by local quantitative measurements of ion current filamentation and magnetic field amplification in interpenetrating plasmas via optical Thomson scattering (TS).<sup>28</sup> What is more, the generation of subrelativistic shocks, together with relativistic electron acceleration, has been demonstrated to be within the reach of larger-scale, NIF-class laser systems.<sup>29</sup>

Another setup relies on a plasma expanding into a preformed ambient magnetized secondary plasma. Thanks to the magnetization, the target ions create a collisionless magnetic piston that accelerates the ambient plasma to super-Alfvénic velocity, thus creating a high-Mach-number shock with velocity of the order of 1000 km/s.<sup>30–33</sup> Recently, Schaeffer *et al.*<sup>34</sup> have been able to make significant progress in characterizing the formation of collisionless shocks in terms of ion and electron density and temperature, as well as electric and magnetic field strengths, as functions of time at OMEGA.

At the LULI laser facility at the École Polytechnique (France), collisionless shock waves and ion-acoustic solitons have been investigated by proton radiography.<sup>35</sup> Moreover, significant electron preheating via lower-hybrid waves has also been achieved in laboratory laser-produced shock experiments with strong magnetic fields, providing a potential mechanism for the famous “injection” problem.<sup>36</sup> Additionally, at the VULCAN laser facility at the Rutherford Appleton Laboratory, temporally and spatially resolved detection of the formation of a collisionless shock has been achieved.<sup>37</sup>

In contrast to the above schemes, novel setups have been used with ultra-high-intensity lasers. For example, at the XingGuang III laser facility at the Laser Fusion Research Center in China, using a short (2 ps) intense ( $10^{17}$  W/cm<sup>2</sup>) laser pulse, an electrostatic (ES) collisionless shock, together with the filaments induced by ion–ion acoustic instability, could be observed via proton radiography.<sup>38</sup>

In our experimental campaigns at JLF/Titan and LULI2000,<sup>39</sup> we investigated shock formation combining laser-produced plasmas, a background medium, and a strong ambient magnetic field (as detailed below). We chose to have an expanding plasma drive a shock into an ambient gas in the presence of a strong external magnetic field. In contrast to Schaeffer *et al.*,<sup>32</sup> in our setup, the expanding plasma and the magnetic field were decoupled as the higher- $Z$  piston evacuated the magnetic field and was thus unmagnetized. This also allowed us to simultaneously have a highly magnetized ambient plasma (with homogeneous and steady magnetic field) and a high- $\beta$  piston (as can be seen in Table I, the plasma thermal  $\beta$  of the piston is  $\beta_{\text{ther}} \equiv P_{\text{ther}}/P_{\text{mag}} \sim 14.0$ ). Moreover, since our magnetic field strength was more than two times higher,<sup>40</sup> reaching 20 T compared with the 8 T in Schaeffer *et al.*,<sup>32</sup> we were able to decouple the electrons more strongly from the ions,<sup>41</sup> and the shock was able to fully separate from the piston, which is crucial for its characterization.<sup>42</sup> As a result, we have been able to characterize the plasma density and temperature, as well as the electric field developed at the shock front, and, more importantly, observe strong nonthermal accelerated proton populations for the first time.

**TABLE I.** Characterized conditions of piston and shock, as well as the calculated parameters. The ion mean free path  $\lambda_{\text{mfp},i} = V_0 \tau_i$ , in which the ion collisional time  $\tau_i = 3m_i^{1/2} (kT_i)^{3/2} / (4\pi^{1/2} n_i Z^4 q_e^4 \ln \Lambda)$ , where  $\ln \Lambda \approx 10$  is the Coulomb logarithm and  $q_e$  is the elementary charge. The Larmor radius  $r_{L,i} = m_i V_0 / (Z q_e B)$ . The ion collisionality is the ratio of the ion mean free path to the Larmor radius. The parameters relative to the piston are measured inside the cavity that is located behind the piston front. The thermal and dynamic beta parameters are the ratios of the plasma thermal and ram pressures, respectively, to the magnetic pressure:  $\beta_{\text{ther}} = P_{\text{ther}} / P_{\text{mag}} = 2\mu_0 n k T / B^2$ , in which  $\mu_0$  is the vacuum permeability and  $k$  is Boltzmann's constant;  $\beta_{\text{dyn}} = P_{\text{dyn}} / P_{\text{mag}} = 2\mu_0 \rho V_0^2 / B^2$ , in which  $\rho = mn$  is the mass density. For the shock, the Mach number is the ratio of the flow velocity to the sound velocity,  $M = V_0 / C_s$ , in which the sound velocity  $C_s = (\gamma Z k T_e / m_i)^{1/2}$ , with  $\gamma = 5/3$ ; the Alfvénic Mach number is the ratio of the flow velocity to the Alfvénic velocity,  $M_A = V_0 / V_A$ , in which the Alfvénic velocity  $V_A = B / (\mu_0 n_i m_i)^{1/2}$ ; and the magnetosonic Mach number is the ratio of the flow velocity to the magnetosonic velocity (see text). For the calculation of the sound velocity and the Alfvénic velocity, we use the parameters of the upstream region.

	Piston region	Shock region
Characterized plasma conditions:		
Averaged atomic number $A$	17.3	1.0
Effective charge state $Z_{\text{eff}}$	8.0	1.0
Electron number density $n_e$ ( $\text{cm}^{-3}$ )	$1.0 \times 10^{19}$	$1.0 \times 10^{18}$
Electron temperature $T_e$ (eV)	80.0	100.0
Ion temperature $T_i$ (eV)	40.0	200.0
Flow velocity $V_0$ (km/s)	1200.0	1500.0
Local magnetic field strength $B$ (T)	5.0	60.0
Upstream magnetic field strength $B$ (T)	...	20.0
Upstream electron temperature $T_e$ (eV)	...	50.0
Upstream ion temperature $T_i$ (eV)	...	20.0
Calculated parameters:		
Ion collisional mean free path $\lambda_{\text{mfp},i}$ (mm)	$6.6 \times 10^{-4}$	10.0
Ion larmor radius $r_{L,i}$ (mm)	5.4	0.3
Ion collisionality $\lambda_{\text{mfp},i} / r_{L,i}$	$1.2 \times 10^{-4}$	37.0
Plasma thermal beta $\beta_{\text{ther}}$	14.0	$3.4 \times 10^{-2}$
Plasma dynamic beta $\beta_{\text{dyn}}$	$5.2 \times 10^3$	2.6
Mach number $M$	...	14.0
Alfvénic Mach number $M_A$	...	3.4
Magnetosonic Mach number $M_{\text{ms}}$	...	3.3

In this paper, we will first show, in Sec. II, that laboratory experiments can be performed to generate and characterize globally mildly supercritical, quasi-perpendicular magnetized collisionless shocks, and detail their characteristics. Then, in Sec. III, we will detail three-dimensional (3D) magnetohydrodynamic (MHD) simulations reproducing the laser-driven piston generation and the subsequent shock formation process. In Sec. IV, with the parameters characterized in the experiment, we will report the results of kinetic particle-in-cell (PIC) simulations, which pinpoint that shock surfing acceleration (SSA) can be effective in energizing protons from the background plasma to 100 keV-level energies.

## II. EXPERIMENTAL SETUP AND RESULTS

### A. Experimental setup

The experiments were performed at the JLF/Titan (LLNL, USA) and LULI2000 (France) laser facilities with similar laser conditions but using complementary diagnostics, with the latter being mostly a consequence of the availability of different auxiliary laser beams at each facility.

In the experiment at JLF/Titan, as shown in Figs. 1(a)–1(c), the collisionless shock was generated by sending a plasma, generated by

having a high-power laser (1  $\mu\text{m}$  wavelength, 1 ns duration, 70 J energy, and  $1.6 \times 10^{13} \text{ W/cm}^2$  on-target intensity) irradiating a solid target (Teflon,  $\text{CF}_2$ ), into a low-density ( $10^{18} \text{ cm}^{-3}$ )  $\text{H}_2$  ambient gas pulsed from a nozzle prior to the shot, and in the presence of a 20 T magnetic field that was homogeneous and steady state on the time scale of the experiment. As shown in Figs. 1(b) and 1(c), the magnetic field, created by a Helmholtz coil system,<sup>40,43</sup> was oriented along the  $y$  or  $z$  axis.

In the subsequent experimental campaign at LULI2000, we set up a similar system, shown in Fig. 1(d). The laser parameters, the ambient  $\text{H}_2$  pressure, and the magnetic field strength were the same as in our previous experiment on Titan and detailed above. In this case, owing to geometrical constraints, the  $\text{CF}_2$  target was tilted by  $60^\circ$  around the  $z$  axis and by  $45^\circ$  around the  $y$  axis, in order to allow the main laser to reach it, as well as to leave access to the Thomson scattering probe beam and collection path.

### B. Density characterization through optical interferometry

Using an interferometry setup,<sup>44</sup> the plasma electron density was recorded by optically probing the plasma (with a mJ, 1 ps auxiliary

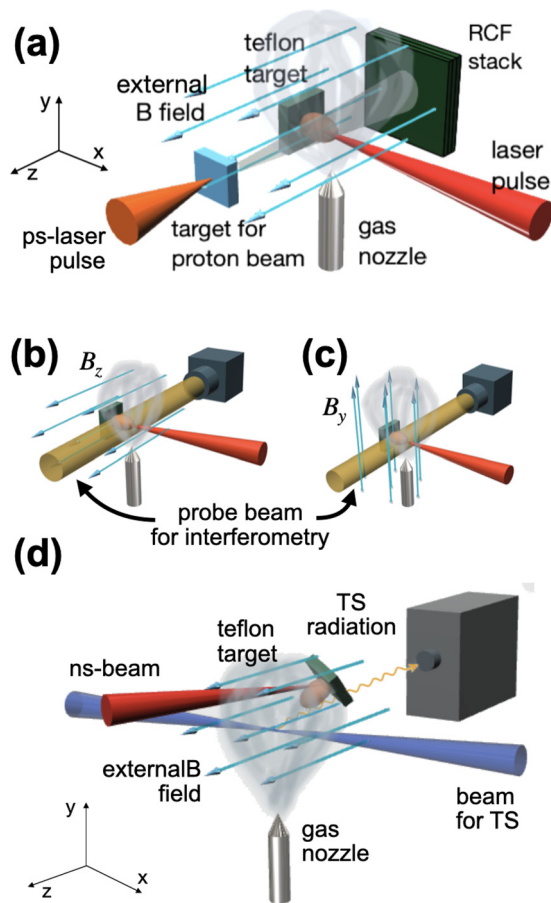


**FIG. 1.** Experimental setup and diagnostics used to characterize a magnetized shock. Proton radiography and interferometry diagnostics were used alternatively along the axis perpendicular to the laser and to the plasma flow (i.e., the  $z$  axis). (a) Proton radiography setup. (b) and (c) In the case of interferometry, we could rotate the coil in order to have two different magnetic field orientations with respect to the field of view of the probe beam. (d) Setup of the Thomson scattering (TS) diagnostic fielded at LULI2000.

laser pulse). In Fig. 2, we present the overall electron density recorded in three different cases.

For the case with both ambient gas and magnetic field shown in Figs. 2(a) and 2(b), the laser irradiation induced the expansion of a hot plasma (the piston) that propagated along the  $x$  axis, and a collisionless shock was formed as a consequence of the plasma piston propagating in the magnetized ambient gas.<sup>32</sup> We can clearly see both the piston front and the shock front (indicated by the orange and green arrows, respectively), and indeed they are well detached from each other, enabling us to characterize them separately.

A lineout of the plasma density is shown in Fig. 2(f), where the piston and shock fronts are also well identified by the abrupt density changes. The piston front is steepened by the compression of the magnetic field (see also below). Besides, we can clearly see a “foot” structure ahead of the shock front in the upstream (US) region for the cases with both ambient gas and magnetic field, indicating the formation of the magnetized shock.<sup>47</sup>

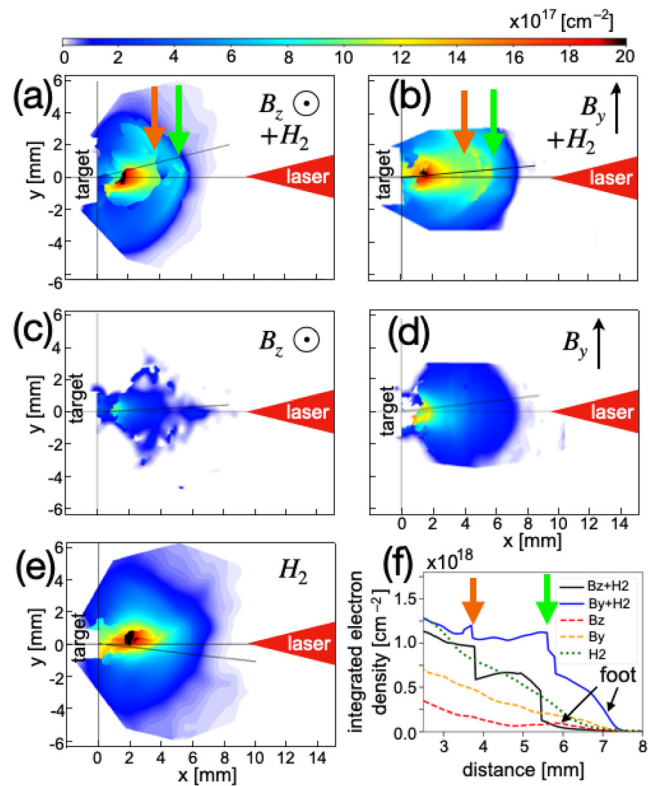


**FIG. 2.** Integrated plasma electron density, as measured by optical probing at 4 ns after the laser irradiation of the target, in three different cases: (a) and (b) with both ambient gas and a magnetic field in the  $xy$  and  $xz$  planes, respectively; (c) and (d) without ambient gas but with a magnetic field in the  $xy$  and  $xz$  planes, respectively;<sup>45,46</sup> (e) with ambient gas but without a magnetic field in the  $xy$  or  $xz$  planes. Each image corresponds to a different laser shot, while the color scale shown at the top applies to all images. The sharp edges on the top and bottom of (b) and (d) are regions blocked by the coil assembly. (f) Lineouts along the thin dark lines shown in each image. The laser comes from the right side and the piston source target is located at the left (at  $x = 0$ ). Orange arrows indicate the piston front, while green arrows indicate the shock front.

By contrast, for the case with only a magnetic field but no ambient gas<sup>45</sup> shown in Figs. 2(c) and 2(d), owing to the lack of ambient gas, no collisionless shock is formed ahead of the piston. For the case with only ambient gas but no magnetic field in Fig. 2(e), again no shock is formed in the ambient gas. From the corresponding lineout in Fig. 2(f), it is clear that only a smooth plasma expansion into the ambient gas (the green dashed line) occurs.

### C. Piston compression characterization through x-ray spectroscopy

To further characterize the piston, the x-ray ion emission of fluorine compressed within the expanding piston was measured by a focusing spectrometer with high spatial resolution (FSSR)<sup>48</sup> at both laser facilities. The FSSR was based on a spherically bent mica ( $2d = 19.9376 \text{ \AA}$ ) crystal with a radius of curvature  $R = 150 \text{ mm}$ . A spatial resolution of  $100 \text{ \mu m/pixel}$  was achieved along the plasma expansion. Image plates (Fujifilm TR BAS) were used as fluorescent

detectors. The implemented scheme resulted in a 13–16 Å spectral range with a high resolution ( $\lambda/d\lambda > 1000$ ). This range covers the spectral lines of fluorine: resonance H-like ( $2p-1$  s transition) and He-like ( $3p-1$  s,  $4p-1$  s,  $5p-1$  s, etc.) transitions, as well as dielectronic satellites to  $Ly_\alpha$ . The diagnostic allowed us to measure electron density and temperature profiles of the piston expansion using a quasistationary approach.<sup>49</sup> The method is based on analyzing the relative intensities of spectral lines of the same charge state and also takes into account the recombining plasma with a “frozen” ion charge.

Figure 3(a) shows that the piston obviously encounters stronger hindrance in the case with both ambient gas ( $H_2$ ) and magnetic field ( $B_z$ ) (see the green diamonds), compared with the other cases, i.e., the case with only  $B_z$  (red dots) and the case with only  $H_2$  (blue triangles). Being time-integrated, the FSSR provides an average on-axis volumetric density over the few tens of nanoseconds when the plasma density and temperature are high, rather than the time-resolved and line-integrated density measured by optical interferometry. These two diagnostics provide complementary views of the piston. We also see in Fig. 3(b) that the electron temperature in the case of  $B_z + H_2$  becomes the highest at the piston front (between 4 and 7 mm), compared with the other cases. In addition, at the position of 4.5 mm, the evaluated electron density for the case of  $B_z + H_2$  is around  $2-3 \times 10^{18} \text{ cm}^{-3}$  and the

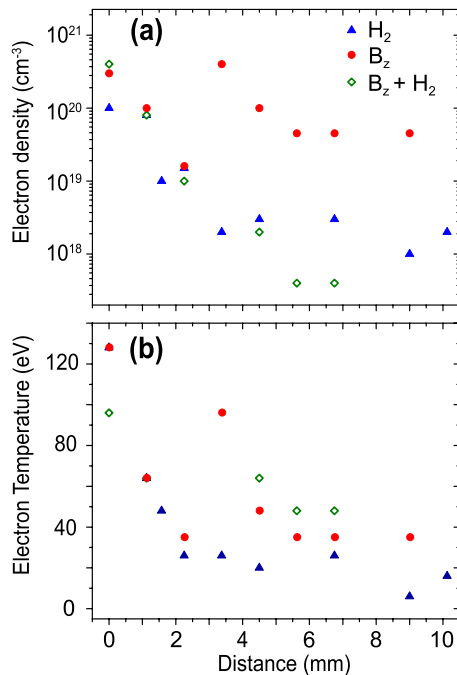


**FIG. 3.** FSSR evaluation of (a) electron density and (b) electron temperature of the laser-produced piston in three different configurations (see legend) along the expansion axis. The measurements are based on analysis<sup>50</sup> of the relative intensities of the x-ray emission lines of He-like and H-like (see text) fluorine ions in the expanding plasma in the range of 13–16 Å. The quasistationary<sup>49</sup> approach was applied for He-like series of spectral lines, assuming a “frozen” ion charge state. The 0 point corresponds to the target surface. A spatial resolution of about 100  $\mu\text{m}$  was achieved. The signal is time-integrated.

electron temperature is about 65 eV, which are reproduced well by our FLASH simulations; see Figs. 8(a) and 8(b).

#### D. Electric field characterization through proton radiography

The single shock front was also probed with protons by measuring the local electric field. The probing protons (accelerated by the target normal sheath acceleration process<sup>51</sup> from an auxiliary target and using the short-pulse arm of Titan) were sent parallel to the magnetic field, i.e., along the  $z$  axis, as shown in Fig. 1(a).

As shown in Fig. 4(a), we can clearly observe the same structures of the piston front and the shock front, consistent with those observed via the optical probe, as shown in Fig. 2.

The synthetic proton radiography shown in Fig. 4(c) is calculated from a particle tracing code, ILZ.<sup>52</sup> ILZ is a test-particle code that uses a given 3D distribution of electric and magnetic fields to simulate the trajectories of the protons as they pass through and then ballistically propagate to the detector.

As an input for the tracing code, we used an electric field  $E_x$  with a bipolar spatial profile along the  $x$  axis with a hemispherical geometry in the  $xz$  plane (where  $z$  is the axis along which the proton beam propagates) in order to imitate the experimentally observed curvature of the shock front. The same dependence on the coordinates  $x$  and  $z$  is

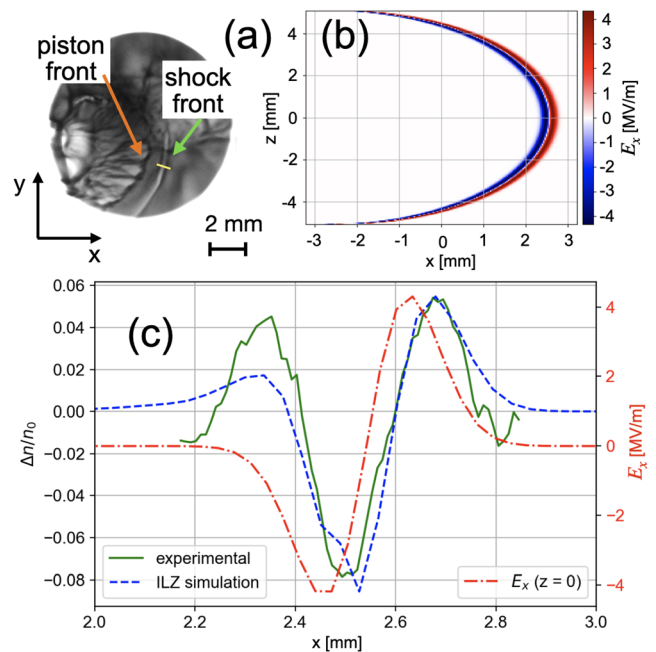


**FIG. 4.** Proton radiography obtained with the setup shown in Figs. 1 and 5 ns after the laser pulse. (a) Raw dose collected on the RCF film corresponding to 19 MeV protons. (b) Hemispherical electric field  $E_x$  in the  $xz$  plane, with a radius  $R = 5.1$  mm, estimated from (a). (c) Lineout of the proton dose modulation along the yellow line in (a). The green full curve is the modulation from the experimental results, and the dashed blue curve is that from the ILZ simulation, which is obtained by imposing a bipolar electric field with hemispherical shape shown in (b). The red dash-dotted curve represents the lineout of the field  $E_x$  in  $z = 0$ .

reproduced along  $y$  over a small thickness. The electric field has only a component along  $x$ , given by

$$E_x(x, z) = \sqrt{2e}E_0 \frac{x - g(z)}{L} \exp\left\{-\frac{[x - g(z)]^2}{L^2}\right\}, \quad (1)$$

where  $E_0$  is the maximum field amplitude and  $L$  represents the width of the region affected by the electric field.  $g(z) = -R/2 + \sqrt{R^2 - z^2}$  represents the shift of  $E_x$  along  $x$  in order to take into account the hemispherical geometry in the  $xz$  plane and derives directly from the equation for a circumference of radius  $R$  centered at  $(-R/2, 0)$ :  $(x + R/2)^2 + z^2 = R^2$ . The hemispherical structure has a radius  $R = 5.1$  mm, which is estimated from the experimental proton radiography relative to that time ( $t = 5.0$  ns after the laser impact), as shown in Fig. 4(a).

We adjust  $E_0$  and  $L$  of the ILZ input in order to match the simulated proton dose with the experimental one. A comparison between these two is shown in Fig. 4(c), where the ILZ-simulated modulation was obtained with the field in Eq. (1) with  $E_0 = 4.33$  MV/m and  $L = 0.12$  mm and is shown in Fig. 4(b).

Note that since the protons are sent along the external magnetic field (i.e., in the  $z$  direction) and since the strength of the magnetic

field components in other directions are orders of magnitude lower than the externally applied one, the Lorentz forces associated with these magnetic field components are much smaller than that induced by the  $E_x$  electric field associated with the shock front. As a result, we interpret the proton dose modulation as being caused by the electric field only. This assumption is supported by the fact that it yields a simulated proton deflection that is highly consistent with the one recorded in the experiment, as can be seen in Fig. 4(c). Also note that the integration time in a given film is too short for motion blurring of the moving shock front to be seen. Additionally, the amplitude of the electric field at the shock front inferred from the synthetic proton radiography is of the order of MV/m. We will compare it with the PIC simulation results and discuss these in detail in Sec. IV.

Furthermore, we compare the position of the shock structure seen in the electron density (via interferometry) with that in the electric field (via proton radiography) for the case with both an external magnetic field and ambient gas. For the former, we consider the point where the electron density has a sharp jump, as shown in Fig. 2(f); for the latter, we take into account the external edges of the proton dose accumulation. Figure 5(a) shows the evolution of the piston front and that of the shock front through both diagnostics (see the caption for details), and they clearly reveal the slowing down of the piston and shock fronts over the first few nanoseconds after the laser pulse. Note that when the target was not clearly visible in the radiography, i.e., for the series of points around 5 ns, we have made use of the interferometry results to shift all the points by the right amount, while keeping the distances between the piston and shock fronts constant. The original radiochromic films (RCFs) for the data points at various times are also shown in Figs. 5(b)–5(e).

### E. Temperature characterization through Thomson scattering

With a second high-energy auxiliary laser (526.5 nm wavelength, 1 ns, 15 J) available at LULI2000, we were able to perform Thomson scattering (TS) off the electron and ion waves in the plasma (used in a collective mode<sup>53</sup> and analyzed by different spectrometers). As shown in Fig. 1(d), the collection of the scattered light was performed at 90° (along the  $z$  axis) with respect to the incident direction of the laser probe (the  $x$  axis). The light scattered off the ion (TSi) and electron (TSe) waves in the plasma was analyzed by means of two different spectrometers, set to different dispersions (3.1  $\mu\text{m}/\text{nm}$  for TSi and  $7.5 \times 10^{-2}$   $\mu\text{m}/\text{nm}$  for TSe), which were coupled to two streak cameras (Hamamatsu for TSe, and TitanLabs for TSi, both equipped with a S-20 photocathode to be sensitive in the visible part of the spectrum, and both with typical 30 ps temporal resolution), allowing us to analyze the evolution of the TS emission in time. The scattering volumes sampled by the instruments were 120  $\mu\text{m}$  along the  $x$  and  $y$  axes and 40  $\mu\text{m}$  along the  $z$  axis for TSi, and 100  $\mu\text{m}$  along the  $x$  and  $y$  axes and 40  $\mu\text{m}$  along the  $z$  axis for TSe. The analysis of the Thomson-scattered light was performed by comparison of the experimental images (recorded by the streak cameras) with the theoretical curves of the scattered spectrum for coherent TS in noncollisional plasmas, with the instrumental function widths of 5.9 nm for the electron spectrometer and 0.12 nm for the ion spectrometer taken into account. Note that the TS laser probe induces some heating in the hydrogen ambient gas. With the estimate of the electron temperature heated by the TS laser obtained through inverse Bremsstrahlung

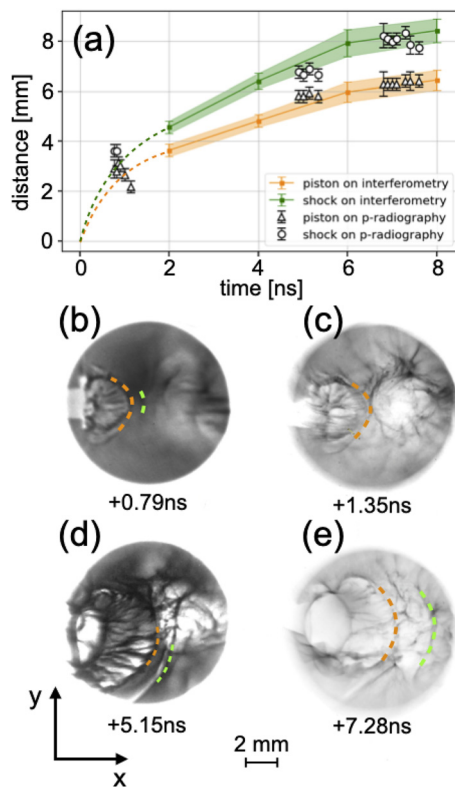


**FIG. 5.** (a) Piston and shock front positions over time from the electron density (via interferometry) and from the electric field (via proton radiography). The full green and orange lines respectively represent the evolution of the shock position and that of the piston location as functions of time as seen on the interferometry diagnostics. They are prolonged toward time 0 by dashed lines passing through the proton radiography data points at  $t \sim 1$  ns. (b)–(e) Images of proton radiography doses at different times, with green and orange dashed lines showing the shock front and piston front, respectively.

absorption, we confirm that the upper limit of the TS-induced heating is only around 60 eV, which is significantly smaller than the level of temperatures we observe in the shock.<sup>39</sup> With the above TS diagnostics, we could access spatially and temporally resolved measurements of the plasma density and temperatures (electron and ion) in the upstream (US), as well as in the downstream (DS) region.

Figure 6 shows the TS measurements in the DS region compared with the shock front for cases with and without an external magnetic field. By comparing the experimental data profiles with the theoretical equation for the scattered spectrum for coherent TS in unmagnetized and noncollisional plasmas, with the instrumental function taken into account, we are able to retrieve the local electron number density, as well as the electron and ion temperatures.<sup>54</sup> For the case without a magnetic field (i.e., with only ambient gas), both TSe and TSi give  $n_e \sim 2.0 \times 10^{18} \text{ cm}^{-3}$  and  $T_e \sim 80 \text{ eV}$ , and TSi also gives  $T_i \sim 50 \text{ eV}$  in the DS region, as can be seen in Figs. 6(a) and 6(c). However, for the case with  $B = 20 \text{ T}$ , we see strong heating in the DS region, indicated by the higher temperatures, i.e.,  $T_e \sim 230 \text{ eV}$  and  $T_i \sim 250 \text{ eV}$ , as can be seen in Figs. 6(b) and 6(d).

Note that with a multi-ionic approach (i.e., including C, F, and H ions), the theoretical scattering curves are calculated from the distribution functions of each species, weighted by their presence fraction. Owing to the natural damping of the other ion species

modes, we observe only one mode in the ion-acoustic wave (IAW) signal.

With all the above diagnostics, we summarize the characterization of the piston and shock conditions in Table I. Note that for the collisionality, the local magnetic field strength is used. Specifically, the local magnetic field strength of the piston is taken from our FLASH simulation results (see Sec. III) and that of the shock is from our PIC simulations, while for the calculation of the Mach numbers for the shock, the parameters of the US region are used.

## F. Evidence for proton energization

For observation of the nonthermal proton spectrum, we used a standard magnetic spectrometer, equipped with permanent magnets of 0.5 T strength and a pinhole. It was located close to the target (17.5 cm away) in order to maximize its collection efficiency, and it had its main axis along  $z$ , the main axis of the external magnetic field (in an alternate mode to performing TS). Note that having the spectrometer collection axis aligned with that of the magnetic field allows measurement of the ions energized out of the plasma,<sup>43</sup> which otherwise could not have been recorded, since they would have been deflected away by the 20 T large-scale magnetic field. We also used filters in order to eliminate the possibility that the signal observed in

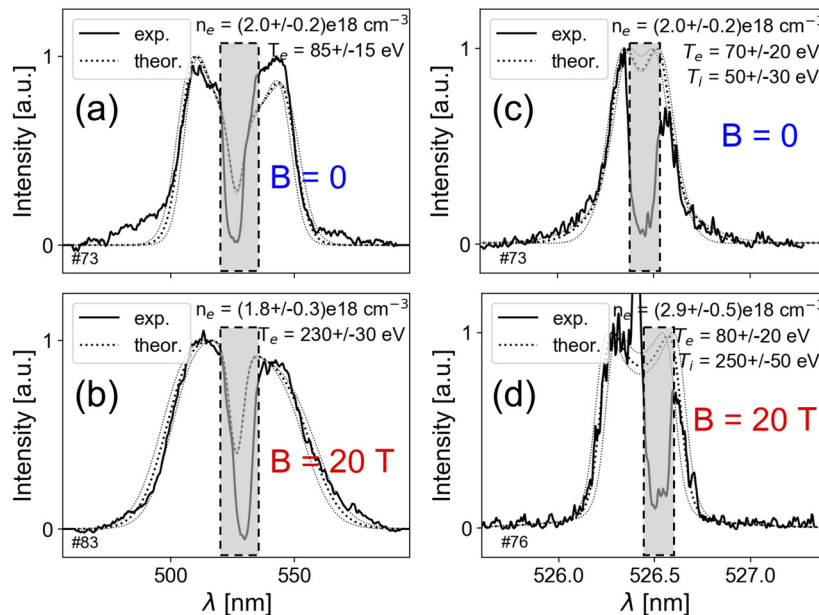


**FIG. 6.** Thomson scattering measurements of the plasma density and temperatures in the region downstream of the shock front for different cases: (a) measurement on the electron waves for the case with  $B = 0$  (i.e., with only ambient gas), allowing retrieval of the local electron number density and electron temperature, as stated; (b) the same measurement for the case with  $B = 20 \text{ T}$  (i.e., with both an external magnetic field and ambient gas); (c) measurement on the ion waves in the plasma for the case with  $B = 0$ , allowing retrieval of the local electron and ion temperatures, as stated; (d) the same measurement for the case with  $B = 20 \text{ T}$ . Solid lines are the experimental data profiles, while dashed lines are the theoretical spectra. The stated uncertainties in the retrieved plasma parameters represent the possible variations of the parameters of the theoretical fit (shown by the thin dotted gray lines). Note that the deep central dip in the experimental spectra is related to a filter (a black aluminum stripe), which was positioned immediately before the entrance of the two streak cameras (recording the light scattered off the electron and ion waves, respectively). This filter was used to block the very intense and unshifted laser wavelength (the Rayleigh-scattered light), which otherwise would have saturated the cameras. Thus, no signal was recorded in this zone, which is indicated by the gray dashed box. The strong narrow peak at around 562.4 nm in (d) is caused by leakage of that strong light just at the edge of the filter. The position of the filter could change in the wavelength domain, because the diagnostic could be realigned between shots.



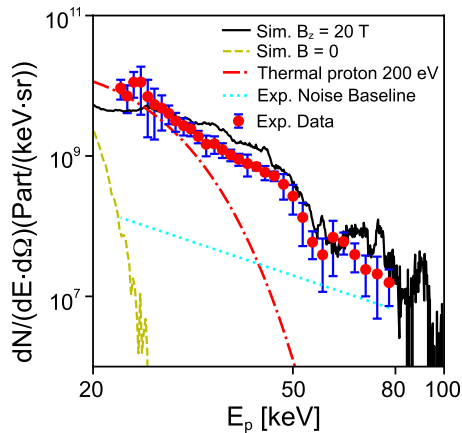


**FIG. 7.** Proton energy spectrum. The experimental data are shown by red dots and blue error bars; the 1D PIC simulation results are shown by the black solid line for the case with  $B = 20$  T and the yellow dashed line for the case with  $B = 0$ ; the analytical thermal proton spectrum is shown by the red dash-dotted line (200 eV); and the experimental noise baseline is shown by the cyan dotted line. Note that the absolute scale in proton numbers (i.e., the number of protons per bin of energy, divided by the solid angle subtended by the entrance pinhole of the spectrometer) applies only to the experimental spectrum; the simulated spectra are adjusted to the experimental one.

the dispersion plane of the spectrometer was originating from heavy ions rather than protons from the ambient gas.

That spectrometer had been calibrated precisely with a Hall probe and on many previous campaigns using filters to verify its energy dispersion. The protons were deflected by the magnetic field inside the spectrometer and landed after a short drift space onto imaging plates (of TR type), the detector used here. These detectors were absolutely calibrated.<sup>55</sup>

The recorded proton spectrum is shown in Fig. 7 by red dots and blue error bars (corresponding to a one-sigma deviation from the average of five shots). On comparing it with the analytical thermal proton spectra (200 eV shown by red dash-dotted lines, as observed in Ref. 39 through TS), it is clear that the proton energization is non-thermal. The cutoff energy reaches about 80 keV.

Note that there is no signal recorded above the noise baseline for cases with only the magnetic field or the ambient gas, indicating that the nonthermal particle populations are indeed coming from the shock. We will pinpoint the underlying proton acceleration mechanism with dedicated PIC simulations in Sec. IV.

### III. MHD SIMULATIONS WITH FLASH

We use the 3D MHD code FLASH<sup>56</sup> to study the dynamics of the plasma plume expansion and piston formation in the ambient gas with a strong magnetic field, using the same parameters as the JLF/Titan experiment. Note that the piston is collisional and is modeled with a MHD code here; whereas the shock is collisionless and is modeled with a kinetic PIC code in Sec. IV. The simulations are initialized in a 3D geometry, using three temperatures (two for the plasma and one for the radiation) with the equation of state of Kemp and Meyer-ter-Vehn<sup>57</sup> and radiative transport, in the framework of

ideal MHD and including the Biermann battery mechanism of magnetic field self-generation in plasmas.<sup>58</sup> Specifically, the laser beam is normal to a Teflon target foil and has an on-target intensity of  $10^{13}$  W/cm<sup>2</sup>, and the generated plasma plume expands in a hydrogen gas jet having a uniform density of  $10^{18}$  cm<sup>-3</sup>. Moreover, the plume expands in a uniform external magnetic field of 20 T (aligned along the  $z$  axis, as in the experiment).

Figure 8 shows the FLASH simulation results, i.e., the electron density, electron temperature, and ion temperature from FLASH at  $t = 2$  ns (after the laser irradiation), in two different cases (the upper row is for the case with ambient gas but no magnetic field, while the lower row is for the case with both ambient gas and a magnetic field). As FLASH cannot handle a vacuum, we do not have a FLASH simulation for the case with a magnetic field but no ambient gas). We can observe that the structures of both the hydrodynamic piston and the induced shock, which propagates inside the ambient gas, are qualitatively reproduced compared with the experiment, specifically:

The Teflon expanding piston produces a forward shock in the ambient gas (around  $x = 1.4$  mm), as well as a reverse shock inside the Teflon piston (around  $x = 0.8$  mm). The electron density is  $\sim 1.6 \times 10^{18}$  cm<sup>-3</sup> in the forward shock in the gas and increases to  $\sim 5 \times 10^{19}$  cm<sup>-3</sup> in the reverse shock.

The electron temperatures are between 60 and 70 eV in the forward and reverse shocks. Both correspond quite well to what is measured in the experiment (see the FSSR measurements in Fig. 3 and the TS measurements in Ref. 39). The ion temperature is 15 eV in the forward shock and between 80 and 180 eV inside the reverse shock.

With regard to the electron temperature, the FLASH simulation results are two times lower compared with the TS measurements in the DS region shown in Fig. 6, while for the ion temperature, the situation is worse, since this is ten times less in the forward shock compared with the TS measurements. Also note that we have not seen the foot structure ahead of the shock in the FLASH simulations.

Such discrepancies between the MHD simulations and the experiments show the difficulties in reproducing the shock condition in our case. This points to the fact that the shock evolution is dominated by kinetic effects. This is why we have resorted to using PIC simulations, the initial conditions for which are taken from the experimental measurements. Nevertheless, we can still observe that the FLASH simulations reproduce well the dynamics of the piston that induces the shock.

Since FLASH has the ability to model magnetic field generation through the Biermann battery effect, it allows us to assess the importance of this effect in the present configuration. Biermann battery generation of magnetic fields is typically important only close to the target surface (the order of 1 mm), and it is localized over the steep temperature gradients generated by the laser beam and rapidly decays once the laser beam is off (see, e.g., Refs. 59–61). As the shock is induced by the piston in the ambient gas 1 mm away from the target surface after the laser is off ( $\sim 2$  ns), as shown in Fig. 8, the Biermann battery effect is negligible compared with that of the strong externally applied magnetic field.

### IV. KINETIC SIMULATIONS WITH SMILEI

The proton energization via the collisionless shock is modeled with the kinetic PIC code SMILEI.<sup>62</sup> During the interaction between the shock front and the ambient plasma, as the width of the shock

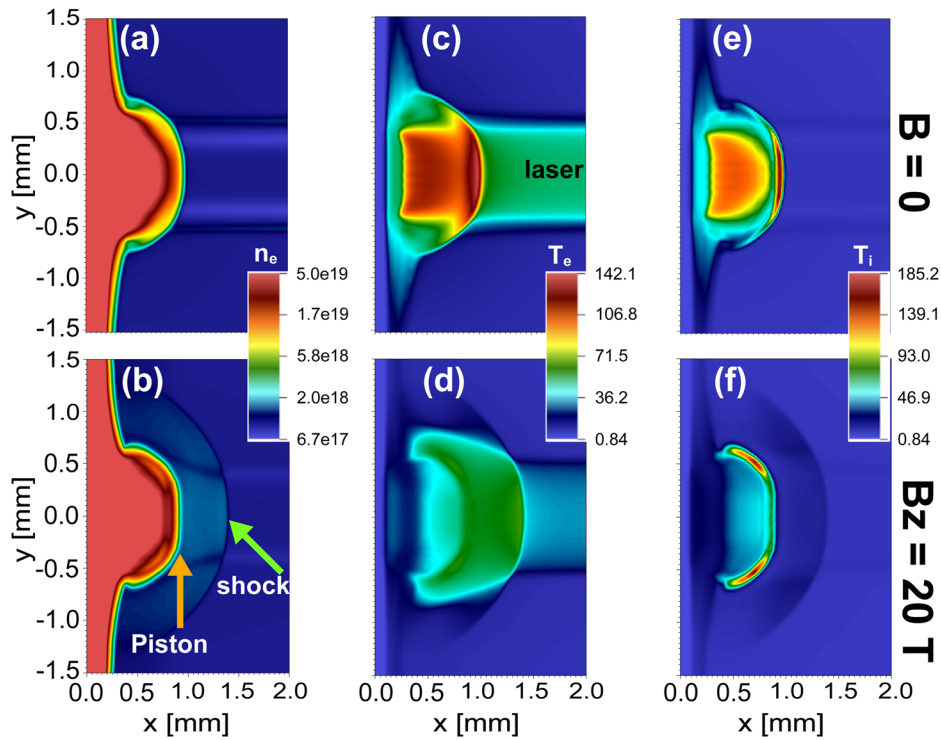


**FIG. 8.** FLASH simulation investigating a single shock formation and performed under the conditions of the JLF/Titan experiment. Maps were extracted from FLASH simulations at 2 ns (after the laser irradiation) of (a) and (b) electron density  $n_e$  in  $\text{cm}^{-3}$ , (c) and (d) electron temperature  $T_e$  in eV, and (e) and (f) ion temperature  $T_i$  in eV. The upper row is for the case without a magnetic field, while the lower row is for the case with a magnetic field. All maps are on a linear scale. This  $xy$ -plane slice is cut at  $z = 0$ . The laser comes from the right side along  $y = 0$ , and the target is at the left side. The orange arrow indicates the piston edge, while the green arrow indicates the shock front.

structure (of order millimeters) is much greater than the thickness of the shock (of order micrometers), we can treat this quasi-one-dimensional interaction, or a thin 1D lineout perpendicular to the curved shock (as shown in Fig. 2), via the 1D3V version of the code.

As shown in Fig. 9, the ambient plasma lies in the right half of the simulation box, while the left half is for the shocked plasma, flowing toward the right with an initial velocity  $v_1 = 1500 \text{ km/s}$ . Both plasmas consist of electrons and protons, with the real mass ratio  $m_p/m_e = 1836$ .

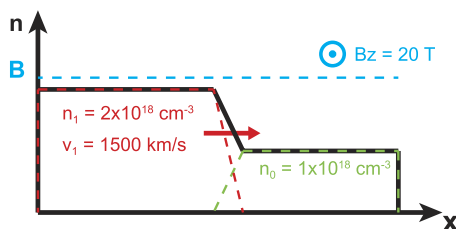


**FIG. 9.** Diagram of PIC simulation setup. The shocked plasma lies in the left half of the simulation box (red dashed line), drifting toward the right, while the ambient plasma lies in the right half (green dashed line). The values of the number density  $n$ , drift velocity  $v$ , and magnetic field  $B$  are indicated. We stress here that the shock width is initialized to be equal to the ion inertial length  $d_i = 200 \mu\text{m}$ .

The simulation box size is  $L_x = 2048d_e = 11 \text{ mm}$ , and the spatial resolution is  $d_x = 0.2d_e = 1.1 \mu\text{m}$ , in which  $d_e = c/\omega_{pe} = 5.3 \mu\text{m}$  is the electron inertial length, with  $\omega_{pe} = (n_{e0}q_e^2/m_e\epsilon_0)^{1/2} = 5.6 \times 10^{13} \text{ s}^{-1}$  being the electron plasma frequency. Here,  $c$  is the speed of light,  $n_{e0} = 1.0 \times 10^{18} \text{ cm}^{-3}$  is the electron number density of the ambient plasma, and  $m_e$ ,  $q_e$ , and  $\epsilon_0$  are the electron mass, elementary charge, and permittivity of free space, respectively. Note that the shock width is initialized to be equal to the ion inertial length  $d_i = 200 \mu\text{m}$ . The magnetic field is homogeneously applied in the  $z$  direction with  $B_z = 20 \text{ T}$  ( $\omega_{ce}/\omega_{pe} = 0.06$ , where  $\omega_{ce} = q_e B/m_e$ ). The simulation lasts for  $1.5 \times 10^5 \omega_{pe}^{-1} \sim 2.5 \text{ ns}$ . Inside each cell, we put 1024 particles for each species. From the perspective of the ion Larmor motion, the simulation size is more than  $10r_{Li}$  in which  $r_{Li} = v_1/\omega_{ci} = m_p v_1/q_e B \sim 0.8 \text{ mm}$ .

For the shocked plasma, the electron number density is  $n_{e1} = 2n_{e0} = 2.0 \times 10^{18} \text{ cm}^{-3}$ , and the temperatures are  $T_{e1} = 100 \text{ eV}$  and  $T_{i1} = 200 \text{ eV}$ , all inferred from the TS characterization.<sup>39</sup> The boundary conditions for both particles and fields are open, and sufficient room is left between the boundary and the shock that the boundary conditions do not affect the physics of interest. Given the initial low temperature of the ambient plasma in the simulation ( $T_{e0} = 50 \text{ eV}$ ), the Debye length is small compared with the grid resolution  $d_x$ , i.e.,  $\lambda_{De} = (\epsilon_0 k T_{e0}/n_{e0} q_e^2)^{1/2} \approx 0.01d_e = 0.05d_x$ . However, we do run a series of simulations with different initial temperatures, showing that the energy conservation for those cases is

limited around 0.05% and the physical results are almost the same. The mean free path of the presented case is  $\lambda_{mfp} \approx 1800d_e$ , which is larger than the interaction scale, further confirming that the shock is collisionless.

We report in Fig. 10 the results of two PIC simulations, namely, with and without a magnetic field. For the case with an applied magnetic field (the left column), typical structures of a supercritical quasi-perpendicular collisionless shock can be seen.<sup>8</sup> These include, for example, the overshoot in the DS region (on the left of the red dashed line), the ramps in the shock fronts (both the red dashed line and the cyan dotted line), and the foot in the upstream (US) region, as can be seen in Fig. 10(a). This foot region is formed by the reflected protons at a distance within  $r_{L,i}$  and modulated by the modified two-stream instability.<sup>63</sup> The proton density  $n_i$  in Fig. 10(e) indicates a compression ratio of  $n_{i,DS}/n_{i,US} \approx 4$ , which agrees with the theoretical jump condition prediction.<sup>64</sup> This density profile, together with the transverse electric field  $E_y$  (not shown here), also follows the distribution of the external applied magnetic field  $B_z$ . The longitudinal electric field  $E_x$  in Fig. 10(c) peaks right at the ramps, providing the electrostatic cross-shock potential to trap and reflect the protons, as can be seen in the phase-space distribution in Fig. 10(g). Because the proton reflection is clearly due to  $E_x$  in our case, not to the DS compressed magnetic field,<sup>9</sup> together with the fact that the ion Larmor radius (about 0.8 mm) is larger than the shock width (around 200  $\mu\text{m}$ ), the dominant particle acceleration mechanism is SSA, not SDA. Note that the cyan dotted line indicates one of the periodic shock reformations.<sup>8</sup> On the contrary, for the case without a magnetic field (the right column), the drifting plasma just penetrates through the ambient gas and no shock is formed; thus, no proton energization can take place, which is in accordance with our experimental observation.

We note that the bipolar structure of the  $E_x$  electric field at the front displayed in Fig. 10(c) matches the one that was retrieved from the proton radiography data, as shown in Fig. 4. Such structures seen in the 1D PIC simulations are also verified in the complementary 2D simulations that will be detailed below. Now, we also note that, quantitatively, in Fig. 10(c), the PIC simulation gives an amplitude of the longitudinal electric field  $E_x \sim 5 \times 10^8$  V/m in the shock layer, which is two orders of magnitude higher than the fitting of the proton radiography in Fig. 4(c). This discrepancy regarding the amplitude of the field between the simulation and the experiment may be due to several reasons: first, the bipolar electric field structure fitted in the proton radiography has a size of 0.4 mm, while the  $E_x$  peaks in the PIC simulations are very sharp, with width smaller than 0.02 mm. With a time average of the PIC simulation over 0.2 ns, the  $E_x$  profile around the shock front reaches a size of 0.4 mm, and its value drops to  $2 \times 10^7$  V/m. Second, the PIC simulation represents the tip of the hemispherical expanding shock front at a single slice of the  $z$  direction, where the magnetic field is strictly perpendicular to the plasma flow and the shock is the strongest [as sketched in Fig. 4(b)]. However, the proton radiography covers the whole shock front with an integration along the  $z$  direction. It includes all other plasma flow directions in the  $xz$  plane, which are not perpendicular to the magnetic field and the corresponding shocks are weaker. This is what was already considered in the analysis of the proton radiography data, as shown in Fig. 4. Last, but not least, the amplitude of the electric field decreases with time. In our 1D PIC simulation, the results are at  $t = 2.7$  ns (from the shock formation); while in the experimental case, the proton radiography results are at  $t = 5.0$  ns (from the laser impact). Hence, we can expect the early-time PIC field to be higher than that derived from radiographs taken at a later time.

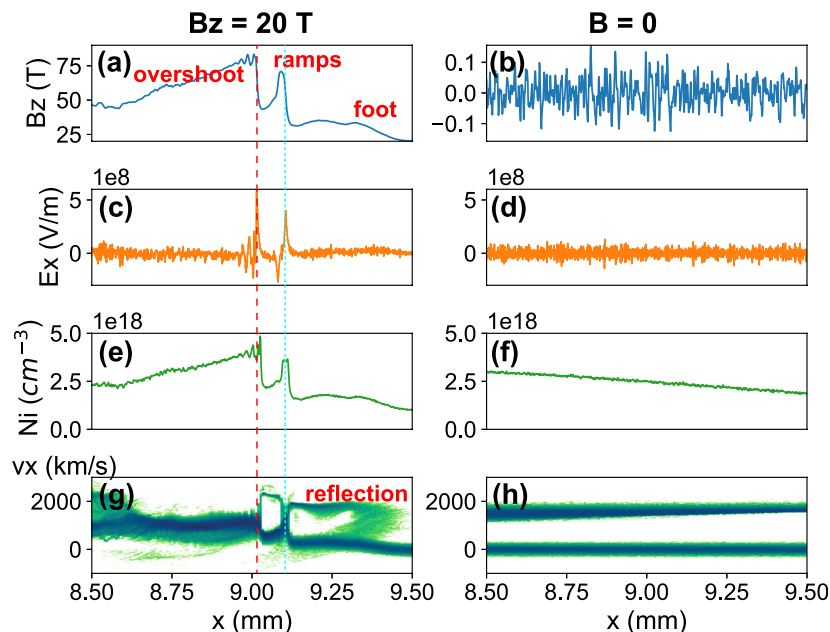


**FIG. 10.** Features of the supercritical quasi-perpendicular collisionless shock structure in ion density and electromagnetic distribution (with and without an external magnetic field), which prove the dominant particle acceleration mechanism to be SSA. (a) and (b) Transverse magnetic field  $B_z$ . (c) and (d) Longitudinal electric field  $E_x$ . (e) and (f) Ion density profile. (g) and (h) Phase-space distribution  $x-v_x$  at the end of the simulation, i.e., at  $t = 2.7$  ns. The left column is for the case with a magnetic field, and the right column is for the case without one. The red dashed line and the cyan dotted line indicate the positions of the shock ramps.

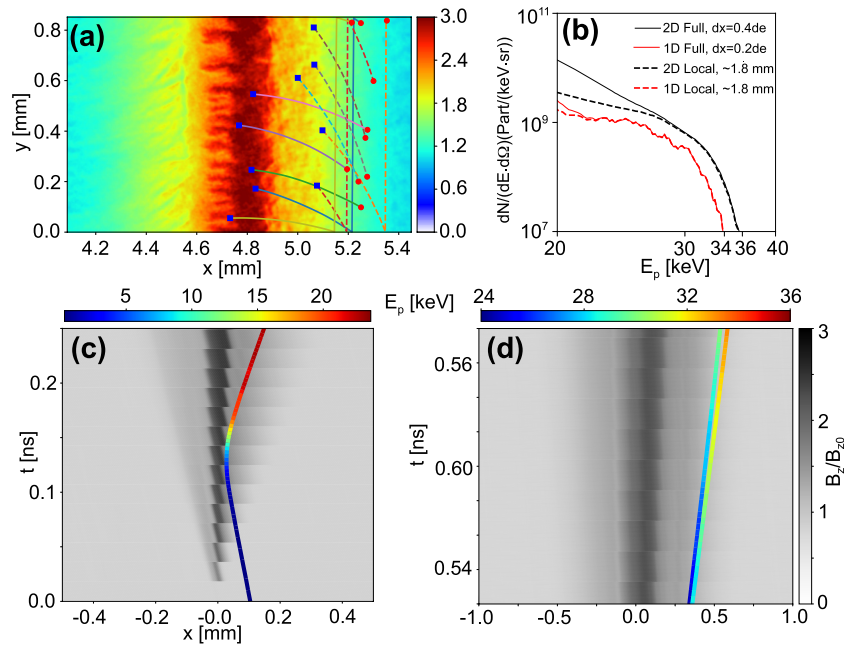


**FIG. 11.** 2D simulation results. (a) Magnetic field maps at 0.7 ns, normalized to 20 T, with trajectories of protons ( $E_k > 30$  keV). Solid lines are for protons from the ambient plasma, and dashed ones are for protons from the drifting plasma; blue squares are the starting positions at 0.5 ns, while red dots are the ending position at 0.7 ns. (b) Energy spectra of both 1D and 2D simulation results at 0.7 ns. Red lines are for the 1D case (solid line for protons in the whole simulation box, dashed line for those that lie around the shock layer in the vicinity of 1.8 mm), while black lines are for the corresponding 2D case. (c) Trajectory of a proton reflected at the shock front in the  $x$ - $t$  diagram, overlaid on the transversely averaged magnetic field map in the reference frame of the contact discontinuity (the gray scale is for the magnetic field strength, while the colored scale is for the proton kinetic energy). (d) Trajectories of two protons surfing along the shock front, also in the  $x$ - $t$  diagram, overlaid on the transversely averaged magnetic field map in the same reference frame.

The particle dynamics of a high-velocity shock (as well as a comparison with the low-velocity case) and of the subsequent shock surfing proton energization are detailed in our previous paper,<sup>39</sup> while here we focus on demonstrating the robustness of the SSA mechanism that is at play in our experiment via 2D simulations, taking the nonstationarity<sup>65</sup> into consideration. Owing to limitations of computational resources, we reduce the 2D simulation scale to an acceptable level: the simulation box sizes are  $L_x = 8$  mm and  $L_y = 0.8$  mm, the simulation time  $t_{\text{end}} = 0.7$  ns, and the resolution  $d_x = 0.4d_e$ .

From Fig. 11(a), we can clearly see that the transverse nonstationarity has already occurred, with 2D stripes mostly positioned at or behind the shock layer, while the trajectories of protons with kinetic energy above 30 keV show that they mainly appear at the shock front, traveling down the negative  $y$  direction. Note that the convective electric field  $\mathbf{E} = -\mathbf{v} \times \mathbf{B}$  is toward the positive  $y$  direction, i.e.,  $E_y = v_x B_z$ , and the drifting of the protons against the convective electric field serves as a distinctive feature indicating that the dominant proton acceleration mechanism is SSA, not SDA.<sup>14</sup> Figure 11(b) shows the proton energy spectra at 0.7 ns in both the 1D and 2D cases, which are close to each other, and there is only a 2 keV difference in the highest-energy cut, which could be caused by the numerical heating in the 2D case (with lower spatial resolution). Moreover, from the energy evolution of the protons in the  $x$ - $t$  diagram, overlaid on the transversely averaged magnetic field map in the reference frame of the contact discontinuity (CD), it can clearly be seen that the accelerated protons are first reflected at (or picked up by) the shock front in

Fig. 11(c) and then surf along the shock front while continuing to gain energy in Fig. 11(d). This is exactly the same picture as we have seen in the 1D simulations,<sup>39</sup> proving that SSA is the dominant proton acceleration mechanism at play (even in the multidimensional case).

Nevertheless, the nonstationarity of the shock might further accelerate the protons at a later time, especially after they have passed through the shock front and gyrate in the DS region. However, unfortunately, right now we do not have the computational resources to reveal that scenario. In short, our 2D simulation shows that the nonstationarity does not prevent the protons from being accelerated by SSA (reflecting and surfing), at least not at early times.

## V. CONCLUSIONS

In conclusion, we have shown that laboratory experiments can be performed to generate and characterize globally mildly supercritical, quasi-perpendicular magnetized collisionless shocks. More importantly, nonthermal proton spectra have been observed for the first time, and the underlying acceleration mechanism has been pinpointed as being SSA via kinetic simulations, which can remarkably reproduce the experimental proton spectra. Such laboratory studies of proton acceleration, as well as those for electrons reviewed above, can not only further our understanding of shock formation and evolution by complementing spacecraft and remote sensing observations, but also help shed new light on solving the fundamental issue of injection for UHECR production.

Our platform can be tuned in the future to perform a systematic study of collisionless shocks with different magnetic field strengths and orientations, enabling us to capture the transition of magnetized collisionless shocks from the subcritical regime to the supercritical one, allowing us to explore the triggering of the other acceleration scenarios (i.e., SDA and DSA).

## ACKNOWLEDGMENTS

The authors would like to thank the teams of the LULI (France) and JLF Laser (USA) facilities for their expert support, as well the Dresden High Magnetic Field Laboratory at Helmholtz-Zentrum Dresden-Rossendorf for the development of the pulsed power generator used at LULI. We thank the Smilei dev-team for technical support; we thank P. Loiseau (CEA-France) for the Thomson scattering analysis code and R. Riquier (CEA, France) for the ILZ code. We also thank Ph. Savoini (Sorbonne University, France), L. Gremillet and C. Ruyer (CEA, France), M. Manuel (General Atomics, USA), and Ph. Korneev (MEPHI, Russia) for discussions. W.Y. would like to thank R. Li (SZTU, China) for discussions. This work was supported by funding from the European Research Council (ERC) under the European Unions Horizon 2020 research and innovation program (Grant Agreement No. 787539). The computational resources of this work were supported by the National Sciences and Engineering Research Council of Canada (NSERC) and Compute Canada (Job Grant No. pve-323-ac). Part of the experimental system is covered by a patent (No. 1000183285, 2013, INPI-France). The FLASH software used was developed, in part, by the DOE NNSA ASC- and the DOE Office of Science ASCR-supported Flash Center for Computational Science at the University of Chicago. We thank J. L. Dubois for providing us EOS and opacities. The research leading to these results is supported by Extreme Light Infrastructure Nuclear Physics (ELI-NP) Phase II, a project co-financed by the Romanian Government and the European Union through the European Regional Development Fund, and by the Project No. ELI-RO-2020-23 funded by IFA (Romania). JIHT RAS team members are supported by the Ministry of Science and Higher Education of the Russian Federation (State Assignment No. 075-00460-21-00). The study reported here was funded by the Russian Foundation for Basic Research, Project No. 19-32-60008.

## AUTHOR DECLARATIONS

### Conflict of Interest

The authors declare no conflicts of interest.

## DATA AVAILABILITY

All data needed to evaluate the conclusions in the paper are present in the paper. Experimental data and simulations are archived on the servers at LULI and LERMA laboratories, respectively, and are available from the corresponding author upon reasonable request.

## REFERENCES

<sup>1</sup>E. A. Helder, J. Vink, C. G. Bassa, A. Bamba, J. A. M. Bleeker, S. Funk, P. Ghavamian, K. J. van der Heyden, F. Verbunt, and R. Yamazaki, "Measuring the cosmic-ray acceleration efficiency of a supernova remnant," *Science* **325**, 719 (2009).

<sup>2</sup>S. Nikolić, G. van de Ven, K. Heng, D. Kupko, B. Husemann, J. C. Raymond, J. P. Hughes, and J. Falcón-Barroso, "An integral view of fast shocks around supernova 1006," *Science* **340**, 45–48 (2013).

<sup>3</sup>D. L. Turner, L. B. Wilson III, T. Z. Liu, I. J. Cohen, S. J. Schwartz, A. Osmane, J. F. Fennell, J. H. Clemmons, J. B. Blake, J. Westlake, B. H. Mauk, A. N. Jaynes, T. Leonard, D. N. Baker, R. J. Strangeway, C. T. Russell, D. J. Gershman, L. Avano, B. L. Giles, R. B. Torbert, J. Broll, R. G. Gomez, S. A. Fuselier, and J. L. Burch, "Autogenous and efficient acceleration of energetic ions upstream of Earth's bow shock," *Nature* **561**, 206–210 (2018).

<sup>4</sup>T. Amano, T. Katou, N. Kitamura, M. Oka, Y. Matsumoto, M. Hoshino, Y. Saito, S. Yokota, B. L. Giles, W. R. Paterson *et al.*, "Observational evidence for stochastic shock drift acceleration of electrons at the Earth's bow shock," *Phys. Rev. Lett.* **124**, 065101 (2020).

<sup>5</sup>R. B. Decker, S. M. Krimigis, E. C. Roelof, M. E. Hill, T. P. Armstrong, G. Gloeckler, D. C. Hamilton, and L. J. Lanzerotti, "Mediation of the solar wind termination shock by non-thermal ions," *Nature* **454**, 67–70 (2008).

<sup>6</sup>F. V. Coroniti, "Dissipation discontinuities in hydromagnetic shock waves," *J. Plasma Phys.* **4**, 265–282 (1970).

<sup>7</sup>J. P. Edmiston and C. F. Kennel, "A parametric survey of the first critical Mach number for a fast MHD shock," *J. Plasma Phys.* **32**, 429–441 (1984).

<sup>8</sup>A. Balogh and R. A. Treumann, *Physics of Collisionless Shocks: Space Plasma Shock Waves* (Springer, New York, 2013).

<sup>9</sup>G. P. Zank, H. L. Pauls, I. H. Cairns, and G. M. Webb, "Interstellar pickup ions and quasi-perpendicular shocks: Implications for the termination shock and interplanetary shocks," *J. Geophys. Res.: Space Phys.* **101**, 457–477, <https://doi.org/10.1029/95ja02860> (1996).

<sup>10</sup>B. Lembège, J. Giacalone, M. Scholer, T. Hada, M. Hoshino, V. Krasnoselskikh, H. Kucharek, P. Savoini, and T. Terasawa, "Selected problems in collisionless-shock physics," *Space Sci. Rev.* **110**, 161–226 (2004).

<sup>11</sup>R. H. Burrows, G. P. Zank, G. M. Webb, L. F. Burlaga, and N. F. Ness, "Pickup ion dynamics at the heliospheric termination shock observed by voyager 2," *Astrophys. J.* **715**, 1109 (2010).

<sup>12</sup>G. P. Zank, J. Heerikhuisen, N. V. Pogorelov, R. Burrows, and D. McComas, "Microstructure of the heliospheric termination shock: Implications for energetic neutral atom observations," *Astrophys. J.* **708**, 1092 (2009).

<sup>13</sup>S. V. Chalov, Y. G. Malama, D. B. Alexashov, and V. V. Izmodenov, "Acceleration of interstellar pickup protons at the heliospheric termination shock: Voyager 1/2 energetic proton fluxes in the inner heliosheath," *Mon. Not. R. Astron. Soc.* **455**, 431–437 (2016).

<sup>14</sup>F. Guo and J. Giacalone, "The acceleration of thermal protons at parallel collisionless shocks: Three-dimensional hybrid simulations," *Astrophys. J.* **773**, 158 (2013).

<sup>15</sup>Z. Yang, Q. Lu, B. Lembège, and S. Wang, "Shock front nonstationarity and ion acceleration in supercritical perpendicular shocks," *J. Geophys. Res.: Space Phys.* **114**, A03111, <https://doi.org/10.1029/2008ja013785> (2009).

<sup>16</sup>Z. Yang, B. Lembège, and Q. Lu, "Impact of the rippling of a perpendicular shock front on ion dynamics," *J. Geophys. Res.: Space Phys.* **117**, A07222, <https://doi.org/10.1029/2011ja017211> (2012).

<sup>17</sup>R. Paul Drake, *High Energy Density Physics: Fundamentals, Inertial Fusion and Experimental Astrophysics* (Springer-Verlag, Berlin, Heidelberg, 2006).

<sup>18</sup>S. Lebedev, A. Frank, and D. Ryutov, "Exploring astrophysics-relevant magneto-hydrodynamics with pulsed-power laboratory facilities," *Rev. Mod. Phys.* **91**, 025002 (2019).

<sup>19</sup>W. Fox, G. Fiksel, A. Bhattacharjee, P.-Y. Chang, K. Germaschewski, S. X. Hu, and P. M. Nilson, "Filamentation instability of counterstreaming laser-driven plasmas," *Phys. Rev. Lett.* **111**, 225002 (2013).

<sup>20</sup>C. M. Huntington, F. Fiuza, J. S. Ross, A. B. Zylstra, R. P. Drake, D. H. Froula, G. Gregori, N. L. Kugland, C. C. Kuranz, M. C. Levy *et al.*, "Observation of magnetic field generation via the Weibel instability in interpenetrating plasma flows," *Nat. Phys.* **11**, 173–176 (2015).

<sup>21</sup>H.-S. Park, C. M. Huntington, F. Fiuza, R. P. Drake, D. H. Froula, G. Gregori, M. Koenig, N. L. Kugland, C. C. Kuranz, D. Q. Lamb *et al.*, "Collisionless shock experiments with lasers and observation of Weibel instabilities," *Phys. Plasmas* **22**, 056311 (2015).

- <sup>22</sup>H.-S. Park, J. S. Ross, C. M. Huntington, F. Fiuza, D. Ryutov, D. Casey, R. P. Drake, G. Fiksel, D. Froula, G. Gregori, N. L. Kugland, C. Kuranz, M. C. Levy, C. K. Li, J. Meinecke, T. Morita, R. Petrasso, C. Plechaty, B. Remington, Y. Sakawa, A. Spitkovsky, H. Takabe, and A. B. Zylstra, "Laboratory astrophysical collisionless shock experiments on omega and NIF," *J. Phys.: Conf. Ser.* **688**, 012084 (2016).
- <sup>23</sup>J. S. Ross, D. P. Higginson, D. Ryutov, F. Fiuza, R. Hatarik, C. M. Huntington, D. H. Kalantar, A. Link, B. B. Pollock, B. A. Remington *et al.*, "Transition from collisional to collisionless regimes in interpenetrating plasma flows on the National Ignition Facility," *Phys. Rev. Lett.* **118**, 185003 (2017).
- <sup>24</sup>C. Courtois, R. A. D. Grundy, A. D. Ash, D. M. Chambers, N. C. Woolsey, R. O. Dendy, and K. G. McClements, "Experiment on collisionless plasma interaction with applications to supernova remnant physics," *Phys. Plasmas* **11**, 3386–3393 (2004).
- <sup>25</sup>D. Yuan, H. Wei, G. Liang, F. Wang, Y. Li, Z. Zhang *et al.*, "Laboratory study of astrophysical collisionless shock at SG-II laser facility," *High Power Laser Sci. Eng.* **6**, E45 (2018).
- <sup>26</sup>Y. Kuramitsu, Y. Sakawa, T. Morita, C. D. Gregory, J. N. Waugh, S. Dono, H. Aoki, H. Tanji, M. Koenig, N. Woolsey *et al.*, "Time evolution of collisionless shock in counterstreaming laser-produced plasmas," *Phys. Rev. Lett.* **106**, 175002 (2011).
- <sup>27</sup>C. K. Li, V. T. Tikhonchuk, Q. Moreno, H. Sio, E. D'Humières, X. Ribeyre, P. Korneev, S. Atzeni, R. Betti, A. Birkel *et al.*, "Collisionless shocks driven by supersonic plasma flows with self-generated magnetic fields," *Phys. Rev. Lett.* **123**, 055002 (2019).
- <sup>28</sup>G. F. Swadling, C. Bruulsema, F. Fiuza, D. P. Higginson, C. M. Huntington, H.-S. Park, B. B. Pollock, W. Rozmus, H. G. Rinderknecht, J. Katz *et al.*, "Measurement of kinetic-scale current filamentation dynamics and associated magnetic fields in interpenetrating plasmas," *Phys. Rev. Lett.* **124**, 215001 (2020).
- <sup>29</sup>F. Fiuza, G. F. Swadling, A. Grassi, H. G. Rinderknecht, D. P. Higginson, D. D. Ryutov, C. Bruulsema, R. P. Drake, S. Funk, S. Glenzer *et al.*, "Electron acceleration in laboratory-produced turbulent collisionless shocks," *Nat. Phys.* **16**, 916–920 (2020).
- <sup>30</sup>D. B. Schaeffer, E. T. Everson, D. Winske, C. G. Constantin, A. S. Bondarenko, L. A. Morton, K. A. Flippo, D. S. Montgomery, S. A. Gaillard, and C. Niemann, "Generation of magnetized collisionless shocks by a novel, laser-driven magnetic piston," *Phys. Plasmas* **19**, 070702 (2012).
- <sup>31</sup>C. Niemann, W. Gekelman, C. G. Constantin, E. T. Everson, D. B. Schaeffer, A. S. Bondarenko, S. E. Clark, D. Winske, S. Vincena, B. Van Compernelle *et al.*, "Observation of collisionless shocks in a large current-free laboratory plasma," *Geophys. Res. Lett.* **41**, 7413–7418 (2014).
- <sup>32</sup>D. B. Schaeffer, W. Fox, D. Haberberger, G. Fiksel, A. Bhattacharjee, D. H. Barnak, S. X. Hu, and K. Germaschewski, "Generation and evolution of high-Mach-number laser-driven magnetized collisionless shocks in the laboratory," *Phys. Rev. Lett.* **119**, 025001 (2017).
- <sup>33</sup>D. B. Schaeffer, W. Fox, D. Haberberger, G. Fiksel, A. Bhattacharjee, D. H. Barnak, S. X. Hu, K. Germaschewski, and R. K. Follett, "High-Mach number, laser-driven magnetized collisionless shocks," *Phys. Plasmas* **24**, 122702 (2017).
- <sup>34</sup>D. B. Schaeffer, W. Fox, R. K. Follett, G. Fiksel, C. K. Li, J. Matteucci, A. Bhattacharjee, and K. Germaschewski, "Direct observations of acoustic dynamics in magnetized collisionless shock precursors in laser-produced plasmas," *Phys. Rev. Lett.* **122**, 245001 (2019).
- <sup>35</sup>L. Romagnani, S. V. Bulanov, M. Borghesi, P. Audebert, J. C. Gauthier, K. Löwenbrück, A. J. Mackinnon, P. Patel, G. Pretzler, T. Toncian *et al.*, "Observation of collisionless shocks in laser-plasma experiments," *Phys. Rev. Lett.* **101**, 025004 (2008).
- <sup>36</sup>A. Rigby, F. Cruz, B. Albertazzi, R. Bamford, A. R. Bell, J. E. Cross, F. Fraschetti, P. Graham, Y. Hara, P. M. Kozlowski *et al.*, "Electron acceleration by wave turbulence in a magnetized plasma," *Nat. Phys.* **14**, 475–479 (2018).
- <sup>37</sup>H. Ahmed, M. E. Dieckmann, L. Romagnani, D. Doria, G. Sarri, M. Cerchez, E. Ianni, I. Kourakis, A. L. Giesecke, M. Notley *et al.*, "Time-resolved characterization of the formation of a collisionless shock," *Phys. Rev. Lett.* **110**, 205001 (2013).
- <sup>38</sup>J. L. Jiao, S. K. He, H. B. Zhuo, B. Qiao, M. Y. Yu, B. Zhang, Z. G. Deng, F. Lu, K. N. Zhou, X. D. Wang *et al.*, "Experimental observation of ion-ion acoustic instability associated with collisionless shocks in laser-produced plasmas," *Astrophys. J. Lett.* **883**, L37 (2019).
- <sup>39</sup>W. Yao, A. Fazzini, S. Chen, K. Burdonov, P. Antici, J. Béard, S. Bolaños, A. Ciardi, R. Diab, E. Filippov *et al.*, "Laboratory evidence for proton energization by collisionless shock surfing," *Nat. Phys.* **17**, 1177–1182 (2021).
- <sup>40</sup>B. Albertazzi, J. Béard, A. Ciardi, T. Vinci, J. Albrecht, J. Billette, T. Burris-Mog, S. N. Chen, D. Da Silva, S. Dittrich *et al.*, "Production of large volume, strongly magnetized laser-produced plasmas by use of pulsed external magnetic fields," *Rev. Sci. Instrum.* **84**, 043505 (2013).
- <sup>41</sup>W. Yao, B. Qiao, Z. Zhao, Z. Lei, H. Zhang, C. Zhou, S. Zhu, and X. He, "Kinetic particle-in-cell simulations of the transport of astrophysical relativistic jets in magnetized intergalactic medium," *Astrophys. J.* **876**, 2 (2019).
- <sup>42</sup>D. B. Schaeffer, W. Fox, J. Matteucci, K. V. Lezhnin, A. Bhattacharjee, and K. Germaschewski, "Kinetic simulations of piston-driven collisionless shock formation in magnetized laboratory plasmas," *Phys. Plasmas* **27**, 042901 (2020).
- <sup>43</sup>D. Higginson, P. Korneev, C. Ruyer, R. Riquier, Q. Moreno, J. Béard, S. Chen, A. Grassi, M. Grech, L. Gremillet *et al.*, "Laboratory investigation of particle acceleration and magnetic field compression in collisionless colliding fast plasma flows," *Commun. Phys.* **2**, 60 (2019).
- <sup>44</sup>D. P. Higginson, G. Revet, B. Khair, J. Béard, M. Blecher, M. Borghesi, K. Burdonov, S. N. Chen, E. Filippov, D. Khaghani *et al.*, "Detailed characterization of laser-produced astrophysically-relevant jets formed via a poloidal magnetic nozzle," *High Energy Density Phys.* **23**, 48–59 (2017).
- <sup>45</sup>B. Khair, G. Revet, A. Ciardi, K. Burdonov, E. Filippov, J. Béard, M. Cerchez, S. N. Chen, T. Gangolf, S. S. Makarov *et al.*, "Laser-produced magnetic-Rayleigh–Taylor unstable plasma slabs in a 20 T magnetic field," *Phys. Rev. Lett.* **123**, 205001 (2019).
- <sup>46</sup>E. Filippov, S. Makarov, K. Burdonov, W. Yao, G. Revet, J. Béard *et al.*, "Enhanced x-ray emission arising from laser-plasma confinement by a strong transverse magnetic field," *Sci Rep.* **11**, 8180 (2020).
- <sup>47</sup>S. Giagkiozis, S. N. Walker, S. A. Pope, and G. Collinson, "Validation of single spacecraft methods for collisionless shock velocity estimation," *J. Geophys. Res.: Space Phys.* **122**, 8632–8641, <https://doi.org/10.1002/2017ja024502> (2017).
- <sup>48</sup>A. Y. Faenov, S. A. Pikuz, A. I. Erko, B. A. Bryunetkin *et al.*, "High-performance X-ray spectroscopic devices for plasma microsources investigations," *Phys. Scr.* **50**, 333–338 (1994).
- <sup>49</sup>S. N. Ryazantsev, I. Y. Skobelev, A. Y. Faenov, T. A. Pikuz, A. N. Grum-Grzhimailo, and S. A. Pikuz, "X-ray spectroscopy diagnostics of a recombining plasma in laboratory astrophysics studies," *JETP Lett.* **102**, 707–712 (2015).
- <sup>50</sup>E. D. Filippov, I. Y. Skobelev, G. Revet, S. N. Chen, B. Khair, A. Ciardi, D. Khaghani, D. P. Higginson, S. A. Pikuz, and J. Fuchs, "X-ray spectroscopy evidence for plasma shell formation in experiments modeling accretion columns in young stars," *Matter Radiat. Extremes* **4**, 064402 (2019).
- <sup>51</sup>S. C. Wilks, W. L. Kruer, M. Tabak, and A. B. Langdon, "Absorption of ultra-intense laser pulses," *Phys. Rev. Lett.* **69**, 1383 (1992).
- <sup>52</sup>S. Bolanos, R. Smets, S. Chen, A. Grisolet, E. Filippov, J. Henares, V. Nastasa, S. Pikuz, R. Riquier, M. Safranov *et al.*, "Laboratory evidence of the halting of magnetic reconnection by a weak guide field," [arXiv:1909.01684](https://arxiv.org/abs/1909.01684) (2019).
- <sup>53</sup>D. H. Froula, N. C. Luhmann, Jr., J. Sheffield, and S. H. Glenzer, *Plasma Scattering of Electromagnetic Radiation: Theory and Measurement Techniques* (Elsevier, 2011).
- <sup>54</sup>D. Froula, J. Ross, B. Pollock, P. Davis, A. James, L. Divol, M. Edwards, A. Offenberger, D. Price, R. Town *et al.*, "Quenching of the nonlocal electron heat transport by large external magnetic fields in a laser-produced plasma measured with imaging Thomson scattering," *Phys. Rev. Lett.* **98**, 135001 (2007).
- <sup>55</sup>A. Mančić, J. Fuchs, P. Antici, S. Gaillard, and P. Audebert, "Absolute calibration of photostimulable image plate detectors used as (0.5–20 MeV) high-energy proton detectors," *Rev. Sci. Instrum.* **79**, 073301 (2008).
- <sup>56</sup>B. Fryxell, K. Olson, P. Ricker, F. X. Timmes, M. Zingale, D. Q. Lamb, P. MacNeice, R. Rosner, J. W. Truran, and H. Tufo, "FLASH: An adaptive mesh hydrodynamics code for modeling astrophysical thermonuclear flashes," *Astrophys. J., Suppl. Ser.* **131**, 273 (2000).
- <sup>57</sup>A. J. Kemp and J. Meyer-ter-Vehn, "An equation of state code for hot dense matter, based on the QEOS description," *Nucl. Instrum. Methods Phys. Res., Sect. A* **415**, 674–676 (1998).
- <sup>58</sup>M. G. Haines, "Magnetic-field generation in laser fusion and hot-electron transport," *Can. J. Phys.* **64**, 912–919 (1986).
- <sup>59</sup>C. K. Li, F. H. Séguin, J. A. Frenje, J. R. Rygg, R. D. Petrasso, R. P. J. Town, P. A. Amendt, S. P. Hatchett, O. L. Landen, A. J. Mackinnon, P. K. Patel, V. A. Smalyuk, T. C. Sangster, and J. P. Knauer, "Measuring E and B fields in laser-produced plasmas with monoenergetic proton radiography," *Phys. Rev. Lett.* **97**, 135003 (2006).

- <sup>60</sup>L. Gao, P. M. Nilson, I. V. Igumenshchev, M. G. Haines, D. H. Froula, R. Betti, and D. D. Meyerhofer, "Precision mapping of laser-driven magnetic fields and their evolution in high-energy-density plasmas," *Phys. Rev. Lett.* **114**, 215003 (2015).
- <sup>61</sup>C. A. Cecchetti, M. Borghesi, J. Fuchs, G. Schurtz, S. Kar, A. Macchi, L. Romagnani, P. A. Wilson, P. Antici, R. Jung, J. Osterholtz, C. A. Pipahl, O. Willi, A. Schiavi, M. Notley, and D. Neely, "Magnetic field measurements in laser-produced plasmas via proton deflectometry," *Phys. Plasmas* **16**, 043102 (2009).
- <sup>62</sup>J. Derouillat, A. Beck, F. Pérez, T. Vinci, M. Chiaramello, A. Grassi, M. Flé, G. Bouchard, I. Plotnikov, N. Aunai *et al.*, "Smilei: A collaborative, open-source, multi-purpose particle-in-cell code for plasma simulation," *Comput. Phys. Commun.* **222**, 351–373 (2018).
- <sup>63</sup>S. Matsukiyo, and M. Scholer, "Modified two-stream instability in the foot of high Mach number quasi-perpendicular shocks," *J. Geophys. Res.: Space Phys.* **108**, 1459, <https://doi.org/10.1029/2003ja010080> (2003).
- <sup>64</sup>L. Woods, in *Shock Waves in Collisionless Plasmas*, edited by D. Tidman and N. Krall (Wiley, New York, 1971).
- <sup>65</sup>D. Burgess and M. Scholer, "Shock front instability associated with reflected ions at the perpendicular shock," *Phys. Plasmas* **14**, 012108 (2007).